Ultrasound-modulated optical tomography: recovery of amplitude of vibration in the insonified region from boundary measurement of light correlation

Hari. M. Varma,[1] Kuriyakkattil P. Mohanan,[2] Nuutti Hyvönen,[1] Akambadath K. Nandakumaran,[3] and Ram M. Vasu[2,*]

[1]*Department of Mathematics, Aalto University, 00076 Aalto, Finland*
[2]*Department of Instrumentation, Indian Institute of Science, Bangalore, 560012, India*
[3]*Department of Mathematics, Indian Institute of Science, Bangalore, 560012, India*
**Corresponding author: vasu@isu.iisc.ernet.in*

Received June 13, 2011; revised September 14, 2011; accepted September 15, 2011; posted September 21, 2011 (Doc. ID 149153); published October 20, 2011

We address a certain inverse problem in ultrasound-modulated optical tomography: the recovery of the amplitude of vibration of scatterers [$p(\mathbf{r})$] in the ultrasound focal volume in a diffusive object from boundary measurement of the modulation depth (M) of the amplitude autocorrelation of light [$\phi(\mathbf{r},\tau)$] traversing through it. Since M is dependent on the stiffness of the material, this is the precursor to elasticity imaging. The propagation of $\phi(\mathbf{r},\tau)$ is described by a diffusion equation from which we have derived a nonlinear perturbation equation connecting $p(\mathbf{r})$ and refractive index modulation [$\Delta n(\mathbf{r})$] in the region of interest to M measured on the boundary. The nonlinear perturbation equation and its approximate linear counterpart are solved for the recovery of $p(\mathbf{r})$. The numerical results reveal regions of different stiffness, proving that the present method recovers $p(\mathbf{r})$ with reasonable quantitative accuracy and spatial resolution.

OCIS codes: 170.3880, 170.3660, 170.7180, 170.3010, 170.4580, 100.3190.

1. INTRODUCTION

Ultrasound-modulated optical tomography (UMOT) [1,2] is an imaging technique that combines the advantages of diffuse optical tomography in producing optical property images with those of ultrasound (US) in producing images of better spatial resolution, because ultrasound scatters very little compared to light in soft tissue. The US, often focused, produces compression and rarefaction in a selected focal volume, the region of interest (ROI) being looked at, causing local refractive index modulation and vibration of the scattering particles [3]. These effects cause light passing through the ROI to be phase modulated and Doppler shifted [4]. These Doppler-shifted so-called "tagged" photons carry local information pertaining to the ROI and, on detection on the boundary of the object, can be used to reconstruct, primarily, the optical contrast of the ROI noninvasively. In the beginning in UMOT, the strength of the detected tagged photons is used to produce a qualitative map of the averaged optical absorption coefficient (μ_a) of the ROI, and a μ_a image is obtained by scanning the object with ultrasound focal volume. The measurement is the modulation depth (M) of the speckle pattern in the exiting near-IR (NIR) light [5], which represents the strength of the tagged photons.

Since a μ_a image, which is organized from the measured M as a gray-level plot, does not contain quantitative information, it has very little diagnostic value. Medical diagnostic imaging should lead to an accurate recovery of optical (μ_a) and mechanical (Young's modulus E) properties of the affected region, from which valuable functional parameters can be ascertained. Therefore, many have attempted to relate M to the optical and mechanical properties of the object through equations. However, the current developments in UMOT stop short of an explicit procedure for quantitative recovery of these useful parameters from M. The aim of the present work is to make a beginning in this direction by recovering the US-induced amplitude of oscillation at the ROI.

One of the first steps in this direction was taken when the effect of the ultrasound on the ROI was modeled in [2,6,7]. It is found that the ultrasound forcing mainly produces a modulation in refractive index (Δn) and an oscillation of the scattering particles at the frequency of the ultrasound. (The modulation produced in the local μ_a is very small and is not considered.) Combined, Δn and the oscillation give a phase modulation to the ultrasound-tagged light, which on interference with the untagged photons produces a speckle pattern whose modulation is dictated by the above-mentioned two effects of the ultrasound forcing. The measured M is also affected by the local μ_a in the ROI.

To finally relate M to μ_a, Δn, and p, one needs a photon transport model that takes into account the effect of perturbation created by the ultrasound. The model which uses light fluence as the basic dependent quantity is insufficient to account for the dynamics of the scattering particles in the ROI. However, in the well-established field known as diffusing wave spectroscopy (DWS) [8,9], one uses models, where the basic quantity of interest is related to the mutual coherence of light, the amplitude correlation $\phi(\mathbf{r},\tau)$. The $\phi(\mathbf{r},\tau)$ is also affected by the dynamics of the particles in the body over and above the optical properties such as μ_a and μ_s (scattering

coefficient). In DWS one studies the temperature driven Brownian motion experienced by the scattering centers. In UMOT, to this scenario we bring in a deterministic dynamics, the oscillations and compressions produced by ultrasound forcing. Therefore, the model of light transport eminently suited in UMOT is the correlation transport equation (CTE) or its diffusive approximation, the correlation diffusion equation (CDE), in both of which the dependent quantity is either a scattering-angle-dependent or angle-averaged $\phi(\mathbf{r},\tau)$. Tomographic recovery with DWS data was attempted in [10,11], and in the context of UMOT, transport models for $\phi(\mathbf{r},\tau)$ have been established through a number of publications in the past [12,13]. In both the CTE and CDE, it is assumed that $k_a l_{\mathrm{tr}} \gg 1$, where k_a is the modulus of the acoustic wave vector and l_{tr} is the transport mean free path [6]. Since the amplitude of vibration in the ROI depends on the elastic properties of the object (i.e., E, assuming the body purely elastic), it is possible to connect the UMOT measurements to Young's modulus of the material in the ROI through $p(\mathbf{r})$ [14].

Our objective in this work is to consider the following inverse problem associated with the UMOT: the recovery of the causes of the phase modulation, Δn, and the amplitude of oscillations from the measured modulation in $\phi(\mathbf{r},\tau)$, $\mathbf{r} \in \partial\Omega$. Here $\partial\Omega$ represents the boundary of the domain Ω. While we have taken into account both these effects in our forward model to compute M, we note that the recovery here is restricted to $p(\mathbf{r})$, leaving a complete recovery of both the parameters to a future publication. Since the tissue is assumed incompressible, and at US excitation of 1 MHz only compressive modes are excited, the change in density (and hence Δn) is, however, quite small. Writing the CDE as a perturbation equation connecting $\phi^{\delta}(\mathbf{r},\tau)$, the perturbations in $\phi(\mathbf{r},\tau)$, to the localized effects introduced by ultrasound, we reformulate the UMOT inversion as a source recovery problem [15]. This recovery of the unknown $p(\mathbf{r})$ [Eq. (12) in Subsection 2.A] is a nonlinear problem due to the appearance of $p(\mathbf{r})$ in the left-hand side (LHS) as well. We have solved for $p(\mathbf{r})$, first linearizing the above equation and then solving the nonlinear equation without recourse to linearization.

We employ a Gauss–Newton scheme [16] to minimize the mean square error between the experimental (here numerically simulated and noise added) and computed measurements, which are derived from $\phi^{\delta}(\mathbf{r},\tau)|_{\mathbf{r}\in\partial\Omega}$. Our measurement M on $\phi^{\delta}(\mathbf{r},\tau)$ is obtained through time Fourier transforming $\phi^{\delta}(\mathbf{r},\tau)$ and taking the modulus of this Fourier transform at $\omega = \omega_a$, the frequency of the ultrasound. The rest of the paper is organized as follows: in Section 2, we describe the CDE for the propagation of $\phi(\mathbf{r},\tau)$ in a tissuelike medium insonified with a focused ultrasound. A nonlinear perturbation model for the perturbations in amplitude autocorrelation induced by the ultrasound is derived from the CDE. A linear perturbation model is also arrived at by linearizing the nonlinear model around $p = 0$. The inverse problem of recovering the function p using the derived nonlinear/linear perturbation models and the measurement M is formulated as a least square minimization problem. The construction of a Jacobian for the measurement with respect to p is discussed in detail in this section for both models. The numerical results showing the recovered image using the least square inversion algorithm are presented in Section 3. Finally, the concluding remarks are given in Section 4.

2. DIFFUSION MODEL FOR THE PROPAGATION OF AMPLITUDE CORRELATION

The background to this work is taken from the publications of Sakadzic and Wang [12,17]. As indicated in Section 1, the model that describes coherent light propagation in a diffusive medium insonified by US is built on the existing models of DWS. The US brings in a local deterministic "dynamics" due to the force applied in the focal volume, resulting in oscillations of scattering particles and a modulation of the refractive index.

Following the outline given in [12], the phase modulations arising in the path due to the two causes are given respectively by

$$\varphi^{o}_{a,b}(t) = \hat{\mathbf{k}}_s \cdot (\mathbf{d}_b(t) - \mathbf{d}_a(t)) \tag{1}$$

and

$$\varphi^{n}_{a,b}(t) = \frac{\eta}{\rho v_a^2} \int_{\mathbf{r}_a}^{\mathbf{r}_b} A(\mathbf{r},t)\mathrm{d}\mathbf{r}, \tag{2}$$

giving the overall phase modulation

$$\varphi_{a,b} = \varphi^{o}_{a,b} + \varphi^{n}_{a,b}. \tag{3}$$

Here, we have considered two typical scattering events from positions $\mathbf{r}_a$ and $\mathbf{r}_b$, which have themselves suffered displacements of $\mathbf{d}_a$ and $\mathbf{d}_b$, and $\hat{\mathbf{k}}_s$ denotes the unit vector along $\mathbf{r}_b - \mathbf{r}_a$. The modulated refractive index is given by $n(\mathbf{r},t) := n_0[1 + \frac{\eta A(\mathbf{r},t)}{\rho v_a^2}]$, where $A(\mathbf{r},t) = A_a \cos(\omega_a t - \mathbf{k}_a \cdot \mathbf{r} + \phi)$ is the assumed plane US pressure wave with A_a being its amplitude, ω_a the angular frequency, $\mathbf{k}_a$ the wave vector, ρ the material density, v_a the US speed, η the elasto-optic coefficient, and ϕ an initial phase. Moreover, $\mathbf{d}_a$ (or $\mathbf{d}_b$) is given by

$$\mathbf{d}_a = \frac{\mathbf{P}_a}{k_a \rho v_a^2} \sin(\omega_a t - \mathbf{k}_a \cdot \mathbf{r}_a + \varphi_{\mathrm{in}}). \tag{4}$$

Here, $\mathbf{P}_a$ is the vector amplitude of oscillation of the scattering particle at $\mathbf{r}_a$ (which is obtained by setting up and solving a momentum balance equation, where the ultrasound forcing and the local elastic properties enter in), ω_a and $\mathbf{k}_a$ are, respectively, the angular frequency and the propagation vector of the ultrasound, and φ_{in} is an initial phase attributed to light.

We track one of the basic coherent properties, namely the specific intensity $I(\mathbf{r},\hat{\mathbf{k}}_s,\tau)$ derived from the mutual coherence function $\langle E_a(\mathbf{r}_a,t) E_b^*(\mathbf{r}_b,t+\tau)\rangle$ expressed in the center of gravity coordinate system. Using Eq. (3) we can find the phase increment $\Delta\varphi(\tau)$ in time τ along the scattering path $\mathbf{r}_b - \mathbf{r}_a$ as $\Delta\varphi(\tau) = \varphi_{a,b}(t+\tau) - \varphi_{a,b}(t)$. Using the assumption that $\mathbf{k}_a l_{\mathrm{tr}} \gg 1$, i.e., when the length scale associated with diffusive light propagation is very large compared to the acoustic wavelength, phase increments contributed from different scattering events are uncorrelated, and therefore $\langle \Delta\varphi \rangle_{l_{\mathrm{tr}}} = 0$. From this we write

$$\langle \exp(j\Delta\varphi) \rangle \approx 1 - |\mathbf{r}_b - \mathbf{r}_a| l_{\mathrm{tr}}^{-1} \frac{\langle \Delta\varphi^2 \rangle_{l_{\mathrm{tr}}}}{2}, \tag{5}$$

where $\langle \Delta\varphi^2 \rangle_{l_{tr}}$ can be computed as in [12]:

$$\langle \Delta\varphi^2 \rangle_{l_{tr}} = |\mathbf{P}_a|^2 \sin^2\left(\frac{\omega_a \tau}{2}\right) \frac{(l_{tr}\mathbf{k}_a \cdot \hat{\mathbf{k}}_s)^2}{1+(l_{tr}\mathbf{k}_a \cdot \hat{\mathbf{k}}_s)^2} \left[S_a^2 (\hat{\mathbf{k}}_s \cdot \hat{\mathbf{k}}_a)^2 + \frac{\eta^2}{(\hat{\mathbf{k}}_s \cdot \hat{\mathbf{k}}_a)^2} - 2\eta S_a\right]. \tag{6}$$

Here S_a, as noted in [12], represents the deviation of the scattering particles' movement in the ROI from the motion of the surrounding material. Since $\mathbf{P}_a$ itself represents the amplitude of oscillation introduced by the ultrasound forcing in the ROI, S_a can be absorbed into $\mathbf{P}_a$. Using Eqs. (5) and (6) one can compute the increment in specific intensity, ΔI, due to scattering from $\mathbf{r}_a$ in the direction $\mathbf{r}_b$ as

$$\Delta I = I(\mathbf{r}_a, \hat{\mathbf{k}}_s', \tau) \exp(-\mu_t |\mathbf{r}_b - \mathbf{r}_a|) \left[1 - |\mathbf{r}_b - \mathbf{r}_a| \mu_t \frac{\langle \Delta\varphi^2 \rangle_{l_{tr}}}{2}\right], \tag{7}$$

where μ_t is the total attenuation coefficient, i.e., $\mu_t = \mu_a + \mu_s$. From Eq. (7) a transport equation for $I(\mathbf{r}_a, \hat{\mathbf{k}}_s', \tau)$ can be derived as

$$\hat{\mathbf{k}}_s \cdot \nabla I(\mathbf{r}, \hat{\mathbf{k}}_s, \tau) = -(\mu_a + \mu_s) I(\mathbf{r}, \hat{\mathbf{k}}_s, \tau) + S(\mathbf{r}, \hat{\mathbf{k}}_s) + \mu_s \int_{4\pi} p(\hat{\mathbf{k}}_s, \hat{\mathbf{k}}_z') \left(1 - \frac{1}{2}\langle \Delta\varphi^2 \rangle_{l_{tr}}\right) I(\mathbf{r}, \hat{\mathbf{k}}_s', \tau) \mathrm{d}\hat{\mathbf{k}}_s'.$$

The above is the CTE derived in [12]. By expanding $I(\mathbf{r}, \hat{\mathbf{k}}_s, \tau)$ in spherical coordinates as $I(\mathbf{r}, \hat{\mathbf{s}}, \tau) = \frac{1}{4\pi}(\phi(\mathbf{r}, \tau) + 3\hat{\mathbf{k}}_s J(\mathbf{r}, \tau))$, one can derive a diffusion-type equation satisfied by $\phi(\mathbf{r}, \tau) = \int I(\mathbf{r}, \hat{\mathbf{k}}_s, \tau) \mathrm{d}\hat{\mathbf{k}}_s$, which is the CDE:

$$-\nabla \cdot D\nabla\phi(\mathbf{r}, \tau) + (\mu_a + \mu_s \hat{\varphi}(\tau))\phi(\mathbf{r}, \tau) = S_0(\mathbf{r}_0), \tag{8}$$

where

$$\hat{\varphi}(\tau) = \frac{1}{2}|\mathbf{P}_a|^2 \sin^2\left(\frac{\omega_a \tau}{2}\right) \left[\eta^2 (k_a l_{tr}) \tan^{-1}(k_a l_{tr}) + \frac{S_a^2}{3} - 2\eta S_a\right].$$

In Eq. (8), $D = 1/(3(\mu_a + \mu_s'))$ is the optical diffusion coefficient and $S_0(\mathbf{r}_0)$ is the isotropic source at $\mathbf{r}_0 \in \Omega$. Equation (8) comes with the boundary condition

$$\phi(\mathbf{r}, \tau) + D\frac{\partial\phi(\mathbf{r}, \tau)}{\partial \mathbf{n}} = 0, \qquad \mathbf{r} \in \partial\Omega.$$

If the Brownian motion caused by temperature is also accounted for, Eq. (8) becomes

$$-\nabla \cdot D\nabla\phi(\mathbf{r}, \tau) + (\mu_a + \mu_s \hat{\varphi}(\tau) + B(\mathbf{r}, \tau))\phi(\mathbf{r}, \tau) = S_0(\mathbf{r}_0),$$

where $B(\mathbf{r}, \tau) = 2\mu_s' k_0^2 D_B \tau$ and D_B is the particle diffusion coefficient at the insonified volume. For simplicity of notation, we use p to denote the quantity $|\mathbf{P}_a|^2$ and call it the amplitude of vibration (in square centimeters). In the absence of ultrasound forcing, the above equation reduces to

$$-\nabla \cdot D\nabla\phi(\mathbf{r}, \tau) + (\mu_a + B(\mathbf{r}, \tau))\phi(\mathbf{r}, \tau) = S_0(\mathbf{r}_0), \tag{9}$$

with the boundary condition

$$\phi + D\frac{\partial\phi}{\partial \mathbf{n}} = 0.$$

Considering the ultrasound probing as a source of perturbation, we rewrite Eq. (8) as Eq. (9) perturbed by the presence of ultrasound forcing in the ROI, causing ϕ to change to $\phi + \phi^\delta$:

$$-\nabla \cdot D\nabla(\phi + \phi^\delta)(\mathbf{r}, \tau) + (\mu_a + B(\mathbf{r}, \tau) + A(\tau)\chi_I p(\mathbf{r}, \tau))(\phi + \phi^\delta)(\mathbf{r}, \tau) = S_0(\mathbf{r}_0), \tag{10}$$

with the boundary condition

$$(\phi + \phi^\delta)(\mathbf{r}, \tau) + D\frac{\partial(\phi + \phi^\delta)(\mathbf{r}, \tau)}{\partial \mathbf{n}} = 0, \qquad \mathbf{r} \in \partial\Omega.$$

Here $A(\tau) = \frac{1}{2}\sin^2(\frac{\omega_a \tau}{2})[\eta^2 (k_a l_{tr}) \tan^{-1}(k_a l_{tr}) + \frac{S_a^2}{3} - 2\eta S_a]$, and χ_I is the characteristic function of the insonified ROI. In UMOT the measurement, M, that is available to reconstruct the function p is the Fourier transform of $\phi(\mathbf{r}, \tau)$ with respect to τ on the object boundary given by

$$M(p, \mathbf{r}, \omega) = \int_0^\infty (\phi + \phi^\delta)(\mathbf{r}, \tau) e^{-j\omega\tau} \mathrm{d}\tau, \qquad \mathbf{r} \in \partial\Omega. \tag{11}$$

Since our objective is to recover the amplitude of vibration introduced by the external force from the ultrasound operating at $\omega = \omega_a$, the most appropriate measurement would be the one based on the Fourier transform of $\phi^\delta(\mathbf{r}, \tau)$, given by

$$\tilde{F}(p, \mathbf{r}, \omega_a)|_{\mathbf{r}\in\partial\Omega} = \int_0^\infty \phi^\delta(\mathbf{r}, \tau) e^{-j\omega_a \tau} \mathrm{d}\tau. \tag{12}$$

From Eq. (12) we get our measurement as $F(p, \mathbf{r}, \omega_a) \approx \tilde{F}(p, \mathbf{r}, \omega_a)$ [18]. In any UMOT experiment, one in fact measures M of Eq. (11) by time Fourier transforming $\phi + \phi^\delta$. However, $\tilde{F}(p, \mathbf{r}, \omega_a)$ can be obtained from such $M(p, \mathbf{r}, \omega_a)$ by removing its background at $\omega = \omega_a$. With this measurement, the UMOT problem can be restated as the recovery of p in the insonified region I given the boundary measurements $\{F\}$. This inverse problem is essentially a nonlinear coefficient recovery problem, which has a linear approximation, wherein it becomes a source recovery problem. We discuss these formulations in the following sections.

A. Nonlinear Perturbation Equation Connecting ϕ^δ and p

The nonlinear perturbation equation connecting ϕ^δ to p is easily derived from Eqs. (9) and (10) as

$$-\nabla \cdot D\nabla\phi^\delta(\mathbf{r}, \tau) + (\mu_a + B(\mathbf{r}, \tau) + A(\tau)\chi_I p(\mathbf{r}, \tau))\phi^\delta(\mathbf{r}, \tau) = -A(\tau)\chi_I p\phi, \tag{13}$$

with the boundary condition

$$\phi^\delta(\mathbf{r}, \tau) + D\frac{\partial\phi^\delta(\mathbf{r}, \tau)}{\partial \mathbf{n}} = 0, \qquad \mathbf{r} \in \partial\Omega. \tag{14}$$

Even though our objective is to recover p from boundary measurements of ϕ^δ, we take a small detour here to discuss the conditions under which ϕ^δ is sufficiently smooth so that convergence of the numerical algorithm for inversion of p is guaranteed. It turns out, as stated in Remark 1 below, that the same conditions also guarantee a smooth enough source due to the perturbation from the ultrasound source. To start with, we assume that the optical and mechanical property distributions satisfy the following conditions: $D_0 \le D \le \bar{D}$, $0 \le D_B \le \bar{D}_B$, $0 \le \mu_a \le \bar{\mu}_a$, and $0 \le B(\mathbf{r},\tau) \le \bar{B}$ for any τ. Here quantities such as $\bar{D}_B$ represent maximum values in the ROI.

Remark 1. With the above assumptions and because $S_0(\mathbf{r}_0)$ in Eq. (9) is a δ-source, one can, through the method of transposition [19], show that there exists $\phi(\cdot,\tau) \in L^2(\Omega)$ that is a unique solution to Eq. (9). In particular, Eq. (9) does not fall within the framework of $H^1(\Omega)$-based variational theory, and thus it cannot be numerically solved by the standard finite element method without considerable refining of the mesh close to $\mathbf{r}_0$. This could present difficulties for the implementation of an iterative least squares reconstruction algorithm, which typically requires repetitive solution of the forward problem. Fortunately, Eq. (13), the forward problem of UMOT, has the unique solution $\phi^\delta(\cdot,\tau) \in H^1(\Omega)$ through the Lax–Milgram lemma, which also demonstrates that Eq. (13) can be solved with the finite element method, circumventing complications due to lack of smoothness.

Allowing a small abuse of notation, we denote by $\mathcal{F}$ the nonlinear operator, which takes p and produces the measurement of Eq. (12), making use of Eqs. (13) and (14). The inversion of $\mathcal{F}$ is posed as the following nonlinear minimization problem:

$$\underset{p\in L^\infty(\Omega)}{\text{minimize}}\ \Theta(p) = \frac{1}{2}\|\mathcal{F}(p) - \mathcal{F}^e\|^2_{L^2(\partial\Omega)} + \frac{\beta}{2}\|p\|^2_{L^2(I)}. \tag{15}$$

Here the second term is a regularization term where $\beta > 0$ is an appropriately chosen regularization parameter and $\mathcal{F}^e$ is the experimental data measured on $\partial\Omega$. A Newton algorithm for the above minimization problem is $p^{(i+1)} = p^{(i)} - H(p^{(i)})^{-1}G(p^{(i)})$, where H and G denote the Hessian and gradient of Θ, respectively, approximated by $H(p)(\delta p) = D\mathcal{F}^*(p)D\mathcal{F}(p)(\delta p) + \beta(\delta p)$ and $G(p) = D\mathcal{F}^*(p)(\mathcal{F}(p) - \mathcal{F}^e) + \beta p$. Also $D\mathcal{F}$ denotes the Fréchet derivative of $\mathcal{F}$ [the composite operator given by Eqs. (12)–(14)] and $D\mathcal{F}^*$ its adjoint. We now proceed to derive an expression for the derivative $\{\frac{\partial\mathcal{F}}{\partial p}\}$ (i.e., the rate of change of measurement with respect to the parameter we would like to recover), from which we can approximate both G and H and set up the Newton iteration to recover p.

The Fréchet derivative of Eq. (13) can be obtained by perturbing p by p^δ, resulting in a perturbation in ϕ^δ, which is denoted by $\phi^{2\delta}$. The equation for the Fréchet derivative is

$$\begin{aligned} &-\nabla\cdot D\nabla\phi^{2\delta} + (\mu_a + B(\mathbf{r},\tau) + A(\tau)\chi_I p)\phi^{2\delta} \\ &\quad = -A(\tau)\chi_I p^\delta(\phi + \phi^\delta), \end{aligned} \tag{16a}$$

with the boundary condition

$$\phi^{2\delta}(\mathbf{r},\tau) + D\frac{\partial\phi^{2\delta}(\mathbf{r},\tau)}{\partial\mathbf{n}} = 0, \qquad \mathbf{r}\in\partial\Omega. \tag{16b}$$

The adjoint of Eq. (16) is given by

$$-\nabla\cdot D\nabla\psi + (\mu_a + B(\mathbf{r},\tau) + A(\tau)\chi_I p)\psi = 0, \tag{17a}$$

with the boundary condition

$$\psi + D\frac{\partial\psi}{\partial\mathbf{n}} = q^+, \tag{17b}$$

where q^+ is a boundary (point) source. Multiplying Eq. (16) by ψ and Eq. (17) by $\phi^{2\delta}$, integrating over Ω and using Green's theorem, we get

$$\int_{\partial\Omega} q^+\phi^{2\delta} = -\int_\Omega A(\tau)\chi_I p^\delta(\phi + \phi^\delta)\psi.$$

For a perturbation $\phi^{2\delta}$ in ϕ^δ, the perturbation in the actual measurement is $\mathcal{F}^{2\delta} = \int_0^\infty \phi^{2\delta}e^{-j\omega_a\tau}\mathrm{d}\tau$. Therefore, the rate of change in the actual measurement $\mathcal{F}$ with respect to p_j, i.e., the value of p around $\mathbf{r}_j \in \Omega$, can be approximated via

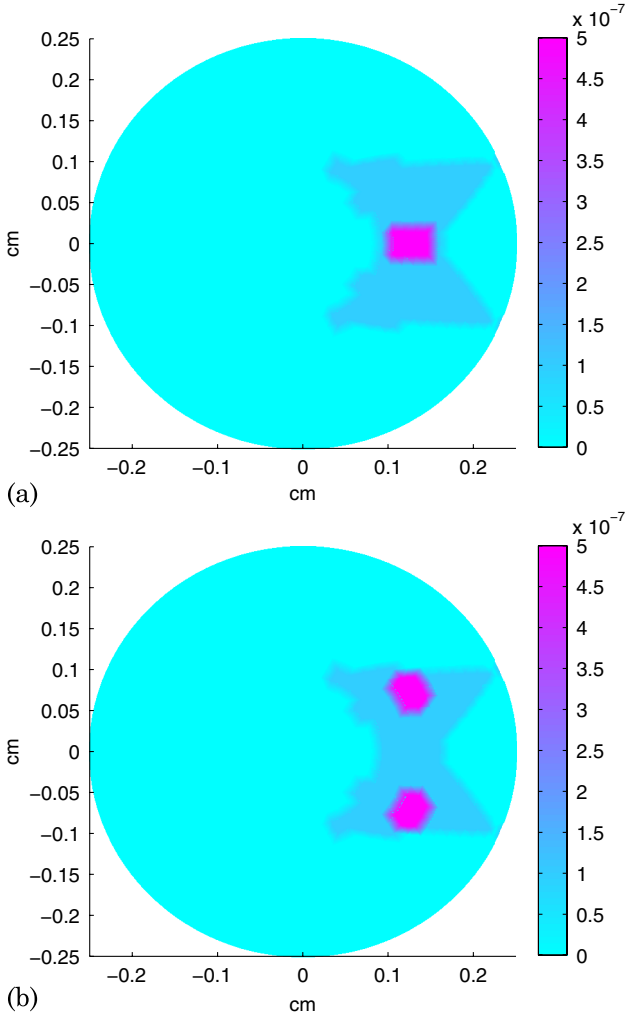

Fig. 1. (Color online) (a) Gray-level image of the object used in the simulations given in terms of $p(\mathbf{r})$ where the insonified region has one inhomogeneous inclusion, (b) gray-level image of the object used in the simulations given in terms of $p(\mathbf{r})$ where the insonified region has two inhomogeneous inclusions.

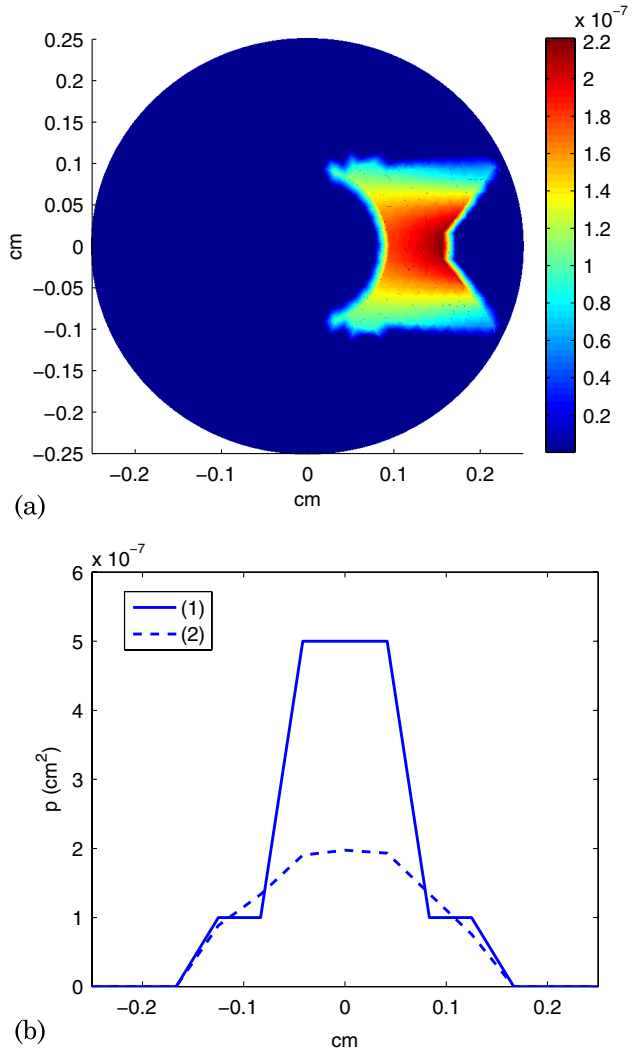

Fig. 2. (Color online) (a) Recovered image obtained from the object of Fig. 1(a) using the nonlinear-perturbation-equation-based algorithm. Data for the algorithm were generated taking refractive index modulation into account as well. (b) Cross-sectional plot through the center of the inhomogeneity in Fig. 2(a) compared with a similar plot from the original in Fig. 1(a).

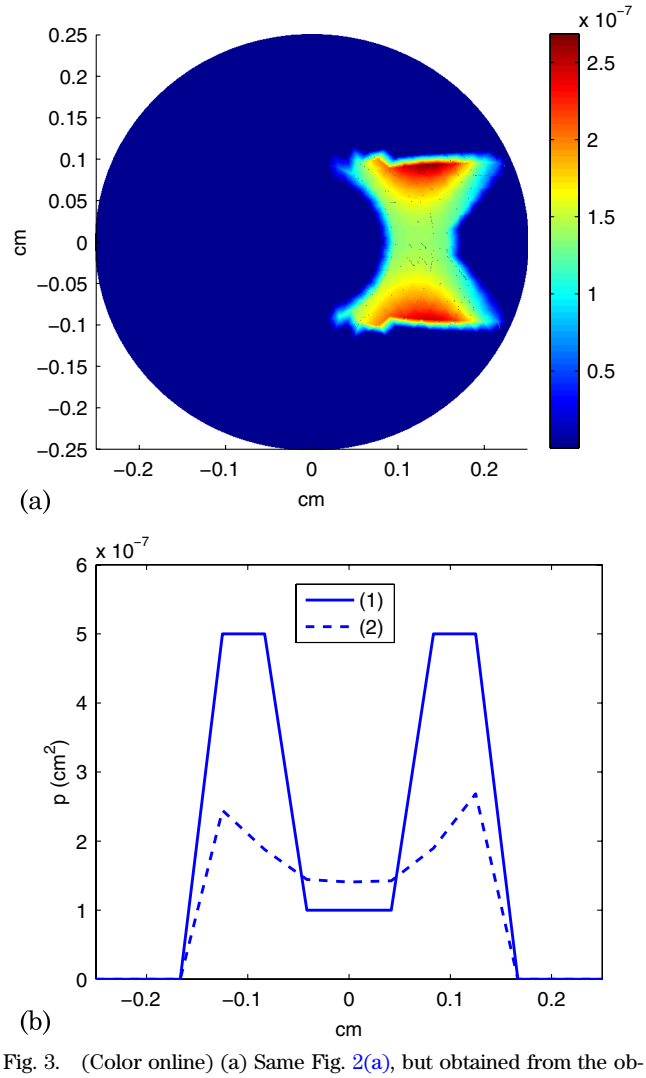

Fig. 3. (Color online) (a) Same Fig. 2(a), but obtained from the object in Fig. 1(b), (b) same Fig. 2(b), but obtained from the reconstructions of Fig. 3(a).

$$\left(\frac{\partial \mathcal{F}}{\partial p_j}\right)_i = -\int_0^\infty [A(\tau)\chi_I(\phi+\phi^\delta)G_R^\psi e^{-j\omega_a\tau}]_{\mathbf{r}=\mathbf{r}_j}\mathrm{d}\tau. \tag{18}$$

Here $G_R^\psi(\mathbf{r},\mathbf{m}_i,\tau)$ is Green's function for the adjoint operator defined by Eq. (17), i.e., $G_R^\psi(\mathbf{r},\mathbf{m}_i,\tau)$ solves Eq. (17) with a boundary source $q^+=\delta_{\mathbf{m}_i}$, a delta source at the ith detector location. Once we have the Jacobian (the finite dimensional equivalent of DF) we can set up an iterative procedure, the details of which are given in earlier publications [20,21].

B. Recovery of p Using a Linearized Perturbation Equation

Neglecting the higher order term $A(\tau)\chi_I p\phi^\delta(\mathbf{r},\tau)$ from the LHS of Eq. (13), we get the following approximate model:

$$\nabla\cdot D\nabla\phi^\delta(\mathbf{r},\tau)-(\mu_a+B(\mathbf{r},\tau))\phi^\delta(\mathbf{r},\tau)=A(\tau)\chi_I p\phi(\mathbf{r},\tau), \tag{19}$$

which is the linearized version of Eq. (13) around $p=0$. However, the inverse problem of recovering p from boundary measurements is still ill posed. Therefore, we take recourse to setting up and solving a least square error minimization problem as in Eq. (15). In the present case, while deriving and implementing the Newton iteration, some simplifications in computation can be effected. For example, the partial differential equation (pde) part [Eq. (19)] of the Fréchet derivative of the forward operator has the same structure as the forward operator pde [Eq. (9)], and therefore, *en route* to implementing the Jacobian, one needs only to use the adjoint of Eq. (9), which is

$$\nabla\cdot D\nabla\psi(\mathbf{r},\tau)-(\mu_a+B(\mathbf{r},\tau))\psi(\mathbf{r},\tau)=0, \tag{20a}$$

along with the boundary condition

$$\psi+D\frac{\partial\psi}{\partial\mathbf{n}}=q^+. \tag{20b}$$

Implementing the variational form of Eq. (19) with ψ [the solution of Eq. (20)] as the test function and imposing the condition given by Eq. (20), we have

$$\int_{\partial\Omega} q^+\phi^\delta=-\int_\Omega A(\tau)\chi_I\psi p\phi. \tag{21}$$

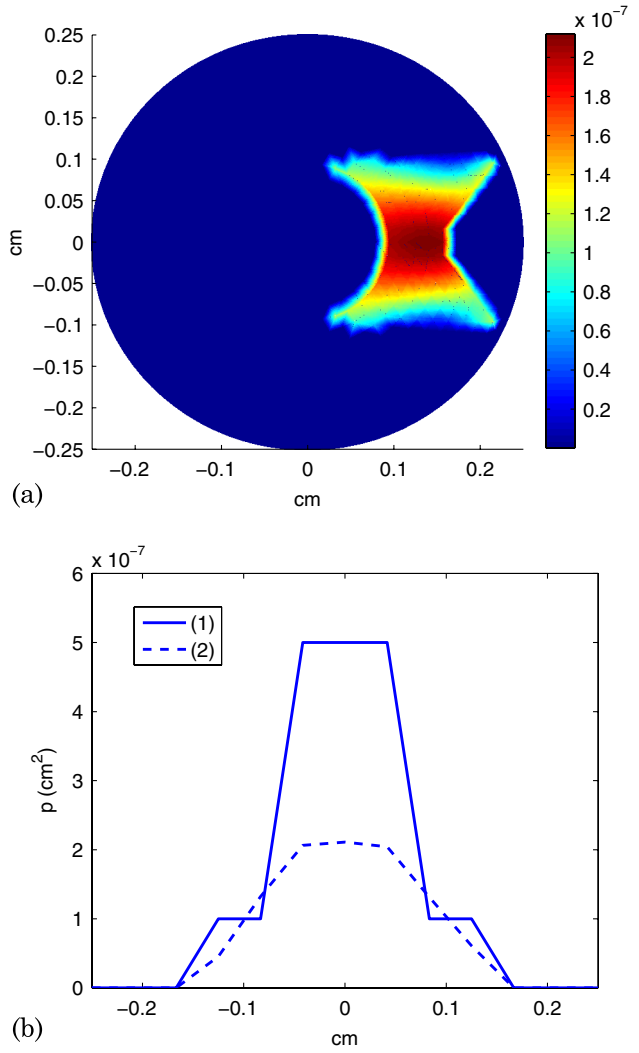

Fig. 4. (Color online) (a) Same as Fig. 2(a), except that data used are generated without taking refractive index modulation into account, (b) cross-sectional plot through the center of the inhomogeneity of the reconstruction in Fig. 4(a).

Taking $q^+ = \delta_{\mathbf{m}_i}$, a delta source at $\mathbf{m}_i \in \partial\Omega$, and using Eq. (21), we can thus approximate the needed Jacobian as

$$\left(\frac{\partial \mathcal{F}}{\partial p_j}\right)_i = -\int_0^\infty [A(\tau)\chi_I \phi G_R^\psi e^{-j\omega\tau}]_{\mathbf{r}=\mathbf{r}_j} \mathrm{d}\tau, \tag{22}$$

where G_R^ψ solves Eq. (20) with $q^+ = \delta_{\mathbf{m}_i}$ and $\mathcal{F}$ still denotes the operator that maps p to the measurement.

Remark 2. In our experience, even though reconstructions based on the nonlinear inverse model of Section 2.A are more accurate than those provided by the linearized version of this section, there seems to be no prominent observable difference in results, except in the case where Δn is included when the linear algorithm failed to converge (see the numerical results in Section 3). When the tissue is assumed incompressible, it is reasonable to neglect Δn. This being true in all practical situations, since the term $A(\tau)\chi_I p\phi^\delta(\mathbf{r},\tau)$ on the LHS of the nonlinear model makes it more involved from the computational point of view, the linearized model introduced above seems adequate to provide a reconstruction in most of the cases.

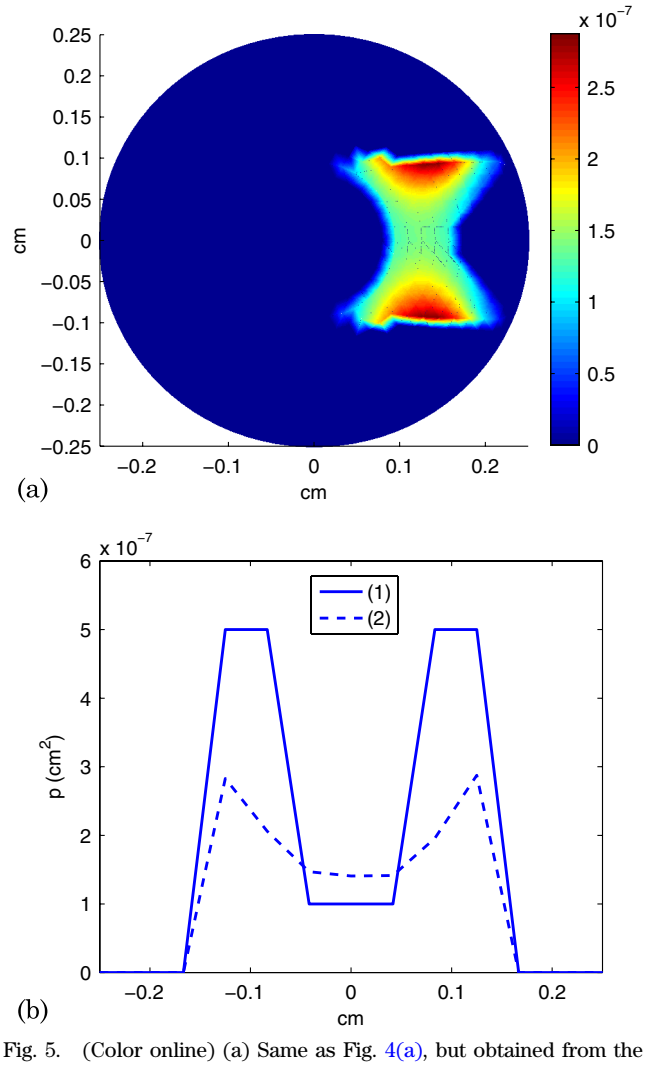

Fig. 5. (Color online) (a) Same as Fig. 4(a), but obtained from the object shown in Fig. 1(b), (b) cross-sectional plot through the center of the inhomogeneities of the reconstruction in Fig. 5(a).

Since the experimental data generation involves finding the Fourier transform of the overall intensity autocorrelation at $\omega = \omega_a$ and removing the bias provided by the temperature-induced Brownian motion, an easier route to compute the forward measurement $\Phi^\delta(\omega_a)$ is by solving the Fourier transform of Eq. (19) for $\Phi^\delta(\omega)$ without the term $B(\mathbf{r},\tau)$, i.e.,

$$-\nabla \cdot D\nabla\Phi^\delta(\omega_a) + (\mu_a + \frac{C_0}{2}\chi_I p)\Phi^\delta(\omega_a) = -\frac{C_0}{2}\chi_I p\pi. \tag{23}$$

We also note that for a proper recovery of p in the ROI it is necessary to have data from multiple source locations, as learned from our numerical simulations.

3. SIMULATION RESULTS AND DISCUSSION

The iterative algorithm starts by solving the forward propagation equation using an initial guess of p, which is the value of p corresponding to the background healthy tissue, which is assumed to be known. At each iteration an update is calculated using the expression

$$\Delta p = (J^T J + \lambda I)^{-1} J^T \Delta\mathcal{F},$$

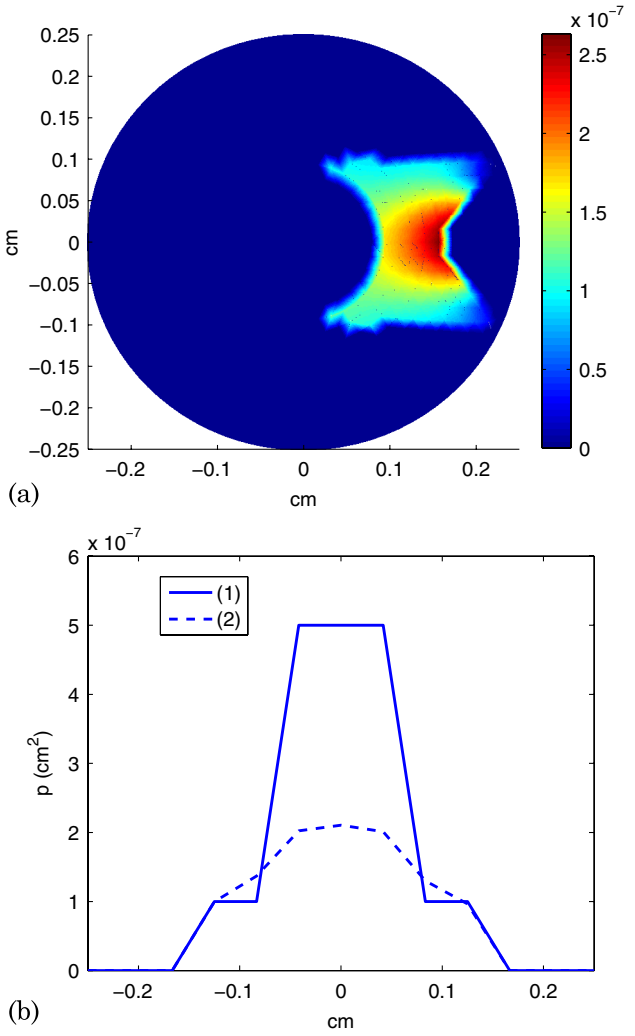

Fig. 6. (Color online) (a) Same as Fig. 4(a), except that the reconstruction algorithm uses the linear perturbation equation, (b) cross-sectional plot through the center of the inhomogeneity of the reconstruction of Fig. 6(a).

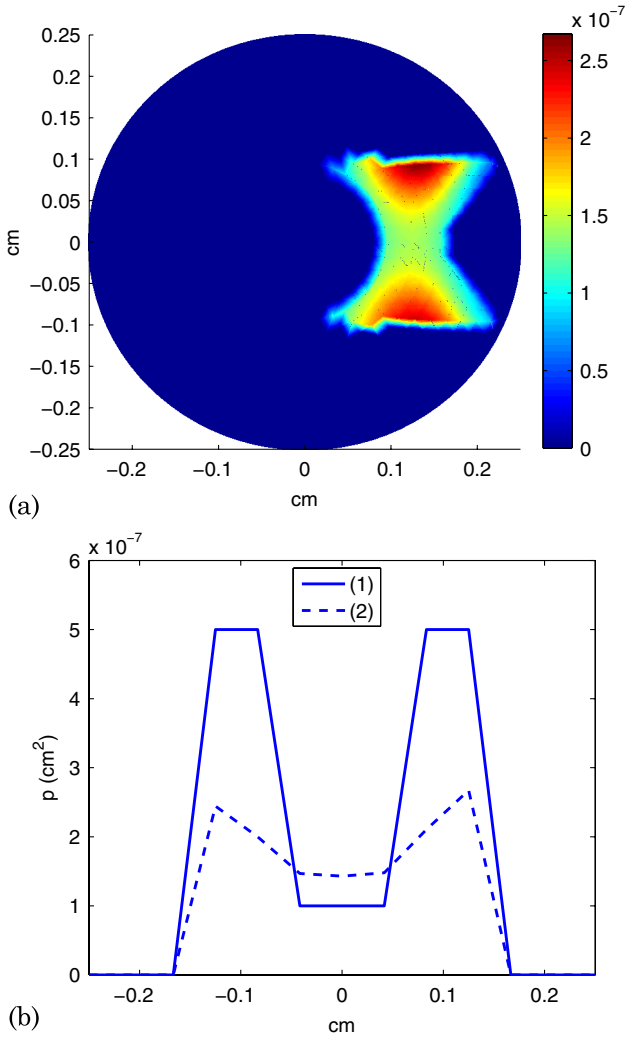

Fig. 7. (Color online) (a) Same as Fig. 6(a), but for the object shown in Fig. 1(b), (b) cross-sectional plot through the center of the inhomogeneity of the reconstruction of Fig. 7(a).

where $\Delta\mathcal{F} = \mathcal{F}^c - \mathcal{F}^e$, $\Delta p = p^{(i+1)} - p^{(i)}$, and J is the Jacobian matrix. Here $\mathcal{F}^c$ is the computed measurement and $\mathcal{F}^e$ is the experimental measurement, which is generated by solving Eqs. (9) and (13) using a finer finite-element mesh and adding noise. In the nonlinear-perturbation-model-based inversion algorithm, Eq. (13) is used as the forward propagation model and the expression in Eq. (18) is used to compute the Jacobian. Since the computation of forward data and the Jacobian depend on τ, the forward problem in Eq. (13) and the adjoint in Eq. (17) have to be solved for each τ. The update is computed for each source position, and this process is iterated several times until the $\|\Delta\mathcal{F}\|$ goes below a certain tolerance level. The same iterative procedure is adopted for the inversion based on the linear perturbation model also, where we solve Eq. (19) to generate the forward data and use Eq. (22) to compute the Jacobian matrix. In this case, the experimental data are generated by solving the nonlinear model in Eq. (13), once again with a finer mesh and adding noise to actually mimic experimental data. As the inverse problem is linear, it is enough to do a one-step inversion that, in principle, should give a good reconstruction of p. However, when the simulations are carried out with only one light source position (a single view from one light source), the algorithm fails to reconstruct p. Therefore, in order to get a proper reconstruction, we have to change the position of the light source and do the inversion for each view in an iterative manner.

The object used for numerical simulations is a circular disc of radius 0.25 cm. The background optical and mechanical properties of the tissue are set as $\mu_a = 0.001\,\mathrm{cm}^{-1}$, $\mu_s' = 20\,\mathrm{cm}^{-1}$, and $D_B = 10^{-9}\,\mathrm{cm}^2$ sec. A two-dimensional cross section of a hyperboloid region centered at (0, 0.125 cm) with waist radius 0.0375 cm and height 0.2 cm is set as the insonified region I, where the amplitude of vibration of scatterers (i.e., p) assumes a value of $1 \times 10^{-7}\,\mathrm{cm}^2$. We consider two cases: the ROI with a single circular inhomogeneous region of radius 0.025 cm centered at the waist and one with two inhomogeneous regions centered at (0.125 cm, 0.07 cm) and (0.125 cm, −0.07 cm), in which the value of p is $5 \times 10^{-7}\,\mathrm{cm}^2$. The ultrasound frequency is set at $f_a = 1$ MHz.

With these objects we have broadly generated two sets of experimental data, one in which Δn is included in the forward operator and the other without this inclusion. For simulating experimental data, we use 1243 nodes and 2376 triangular elements in the finite element method (FEM) discretization of Eq. (13). With this scheme, the FEM with a bilinear basis

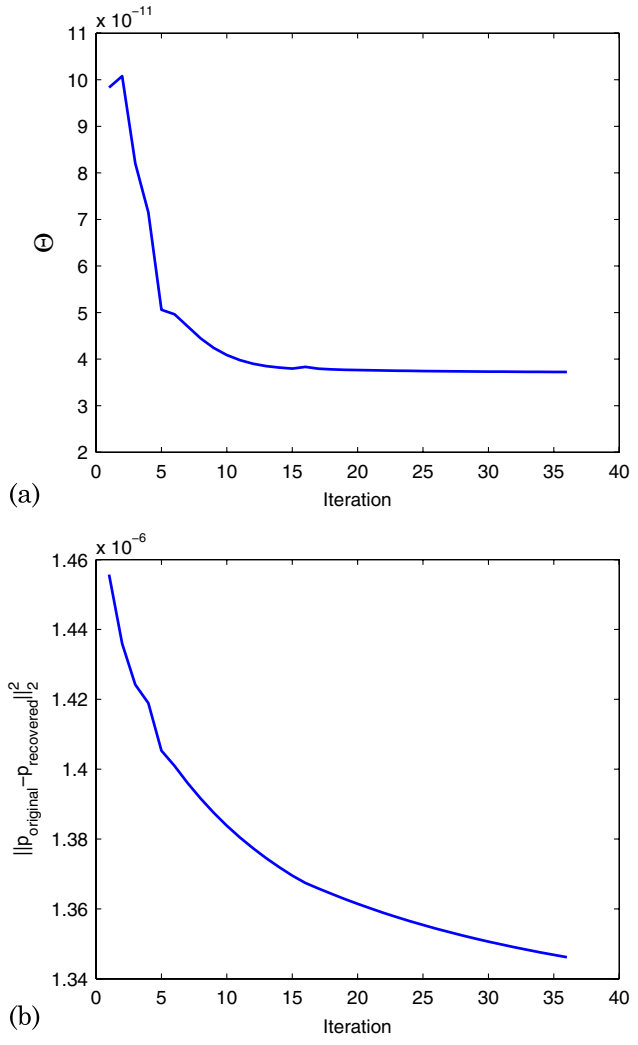

Fig. 8. (Color online) (a) Plot of the data domain error Θ_i versus iteration number, i, for the object given in Fig. 1(b) with refractive index modulation included in the simulation. The reconstruction uses the nonlinear perturbation equation. (b) Plot of the object domain error $\epsilon_i = \|p_{\text{original}} - p_{\text{recovered}}\|_2^2$ versus iteration number, i, for the object given in Fig. 1(b) with refractive index modulation included in the simulation. The reconstruction algorithm uses the nonlinear perturbation equation.

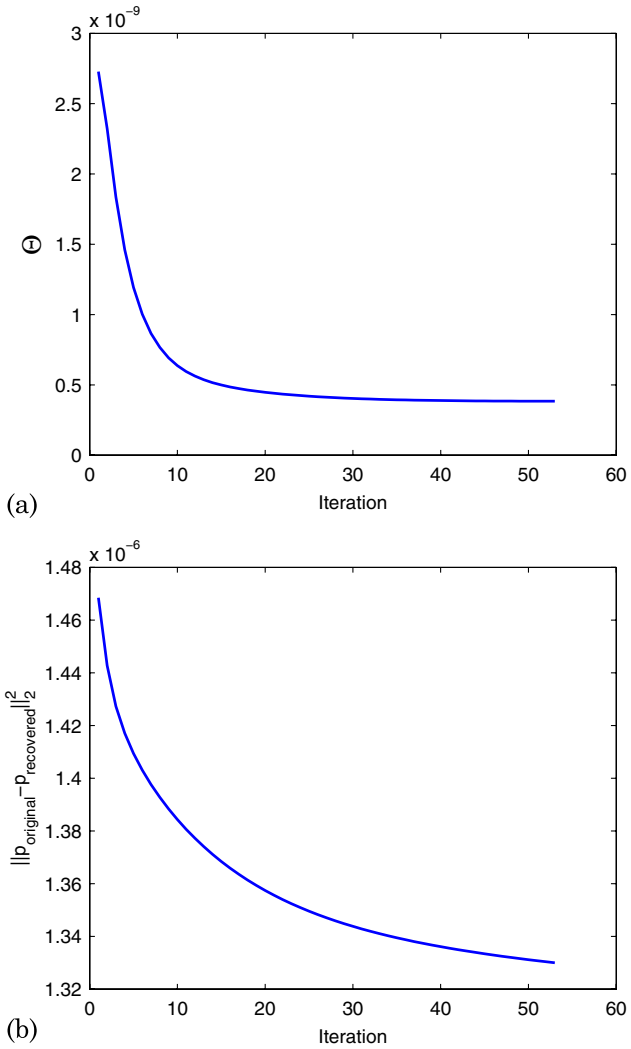

Fig. 9. (Color online) (a) Same as Fig. 8(a), except that data used are generated without taking refractive index modulation into account, (b) same as the one in Fig. 8(b), except that data used are generated without taking refractive index modulation into account.

function is used to generate the forward solution for τ, ranging from 0 s to 5×10^{-7} s with an increment of 5×10^{-8} s. To this ϕ^{δ} at the boundary, we add 1% Gaussian noise and then calculate the measurement $\tilde{F}$ given in Eq. (12) to generate the experimental data for a single source position. In order to get the complete set of experimental data $\mathcal{F}^e$, the above procedure is repeated for each of the source positions obtained by rotating the source and the set of detectors (17 in our case, placed equiangularly, one at the diametrically opposite point to the source and the others on either side of it) by 19 degrees to generate 18 sets of 17 readings each.

To avoid the so-called "inverse crime," we use a coarser mesh for the inversion algorithm consisting of 901 nodal points with 1710 triangular elements. The reconstruction algorithm is initiated with a background value of $p = 1 \times 10^{-7}$ cm^2 in the insonified region I. Since Eqs. (18) and (22) contain the characteristic function χ_I on the right-hand side, the dimension of the Jacobian matrix is $n_I \times m$, where n_I is the number of nodes in the region I and m is the number of detectors. Thus the update is computed only for the region I, and in the UMOT the illposedness is reduced considerably compared to the diffuse optical tomography problem. By trial and error, regularization parameter λ used in the algorithm is fixed for inversions using linear and nonlinear perturbation equations. In the nonlinear case, when Δn is included, the initial λ was kept at 10^{-7} and adaptively reduced by a factor of 2 at each iteration if error Θ_i is less than Θ_{i-1}. The algorithm is terminated when

$$100\left(\frac{\Theta_i - \Theta_{i-3}}{\Theta_{i-3}}\right) < 0.1. \tag{24}$$

For the nonlinear case without Δn, initial λ is 10^{-5} and is kept constant until the stopping criterion mentioned above is met. When the linear perturbation equation is used, the algorithm that took Δn into account, as indicated earlier, did not converge. When Δn is omitted, convergence is obtained by choosing an initial λ of 10^{-8} and decreasing it by half in each iteration when Θ_i is less than Θ_{i-1}.

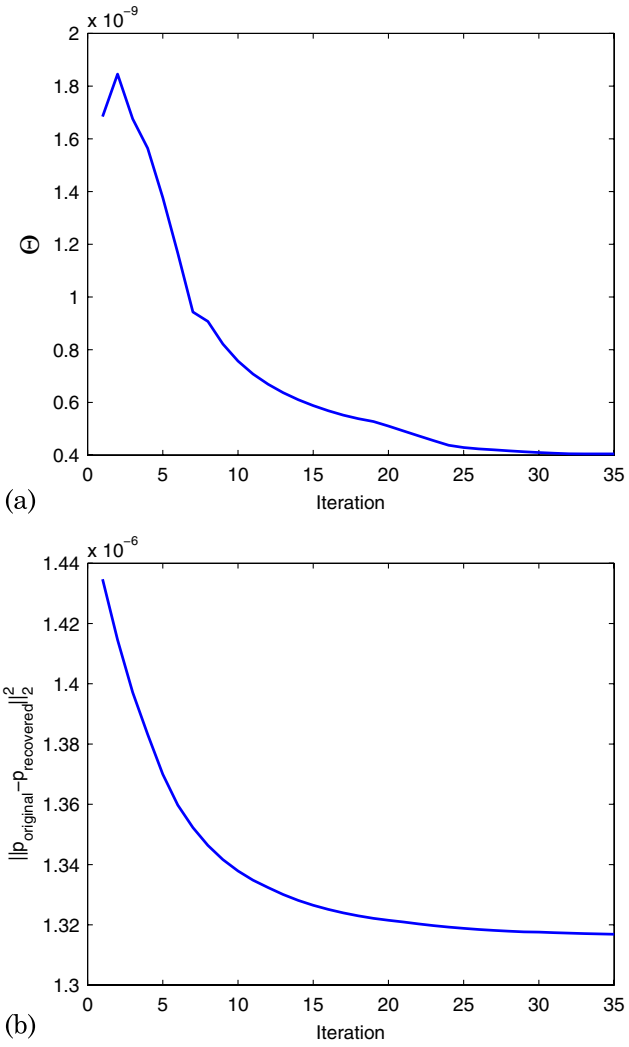

Fig. 10. (Color online) (a) Same as Fig. 9(a), but with the linear-perturbation-based-equation used for inversion, (b) same as Fig. 9(b), but with the linear-perturbation-based-equation used for inversion.

The original distribution of $p(\mathbf{r})$ used to generate the experimental data is shown in Figs. 1(a) and 1(b). For the object given in Fig. 1(a), the recovered $p(\mathbf{r})$, using the nonlinear perturbation equation with Δn included in the data generation step, is shown in Fig. 2(a). A cross-sectional plot through the center of the inhomogeneity for the above reconstruction is shown in Fig. 2(b). For comparison, a cross section across the original object is also shown. When the above data are used in a linear-perturbation-based algorithm, we did not get convergence. Figures 3(a) and 3(b) are similar reconstruction and cross-sectional plots corresponding to the object of Fig. 1(b).

When Δn was not included in the data generation step, we obtained reconstructions with both the linear and nonlinear algorithms. Figures 4 and 5 give reconstructions and cross-sectional plots when the nonlinear algorithm is used against data from Figs. 1(a) and 1(b) respectively. Corresponding reconstructions using the linear algorithms are shown in Figs. 6 and 7. Figures 8(a) and 8(b) show the data domain and object domain error plots (mean square error of the reconstructions with respect to original known object), respectively, for the case when the nonlinear-perturbation-equation-based model is used with refractive index modulation included in the data generation. In this case the data are generated using the object given in Fig. 1(b). Figure 9 is the same as Fig. 8 except that the refractive index modulation is not included in the data generation. The error plots for the linear-perturbation-equation-based inversion algorithm for the object given in Fig. 1(b) are shown in Fig. 10. The position of the inhomogeneity is recovered satisfactorily in all reconstructions, whereas the contrast recovery is generally poor. It is seen that the algorithm is able to reconstruct up to 50% of the original value of p with a reasonably good spatial resolution.

4. CONCLUSIONS

The noninvasive imaging of tissue elastic properties using both light and ultrasound is a very promising hybrid method for the diagnosis of cancer. In this work we have developed a numerical algorithm for noninvasive imaging of amplitude of vibration of scatterers, p, inside a tissuelike medium using a near-IR light source and a focused ultrasound. Two forward propagation models, namely, linear and nonlinear perturbation models, based on the CDE were developed for this purpose. The nonlinear perturbation model was developed by rewriting the CDE for the perturbations in the amplitude correlation induced by the introduction of ultrasound in the light propagation path. The linear perturbation model is then derived from the nonlinear model by linearizing the equation with respect to the function p around zero. We then define a measurement $\tilde{F}$ based on the Fourier transform of the solution of the nonlinear/linear models with respect to correlation time τ. As the inverse problem of recovering p from the function $\tilde{F}$ is an ill-posed problem, we reformulate it as a least square minimization problem. The Hessian and gradient needed for the minimization scheme were approximated for both the nonlinear and linear perturbation models. The algorithm was able to recover the function p up to 50% of the original value for the cases of nonlinear and linear perturbation models. Whereas the nonlinear algorithm is able to produce convergence whether Δn is included in the forward model or not, the linear model gave results only when Δn was not included. The locations of the two inhomogeneities were accurately recovered, thus giving a good spatial resolution of the recovered distribution limited by l^*. One can use the reconstructed $p(\mathbf{r})$ in a momentum balance equation to recover Young's modulus $E(\mathbf{r})$ in the ROI. This $E(\mathbf{r})$ can be used to assess the growth of a tumor and its malignancy. Scaling from two-dimensional to three-dimensional is possible, though not attempted here, provided a pseudodynamic form of the update equation is integrated, avoiding inversion of the ill-conditioned system matrix [21].

ACKNOWLEDGMENTS

The work of H. M. Varma and N. Hyvönen was supported by the Academy of Finland (the Centre of Excellence in Inverse Problems Research and project 135979). A. K. Nandakumaran and R. M. Vasu would like to thank the Council of Scientific and Industrial Resarch for the support under project reference number 25(0194)/11/EMR-II DTD 2.2.11.

REFERENCES AND NOTES

1. L. H. V. Wang, S. L. Jacques, and X. M. Zhao, "Continuous wave ultrasonic modulation of scattered laser light to image objects in turbid media," Opt. Lett. **20**, 629–631 (1995).
2. M. Kempe, M. Larionov, D. Zaslavsky, and A. Z. Genack, "Acousto-optic tomography with multiply scattered light," J. Opt. Soc. Am. A **14**, 1151–1158 (1997).
3. L. V. Wang, "Mechanisms of ultrasonic modulation of multiply scattered coherent light: an analytic model," Phys. Rev. Lett. **87**, 043903 (2001).
4. G. Yao and L. V. Wang, "Theoretical and experimental studies of ultrasound-modulated optical tomography in biological tissue," Appl. Opt. **39**, 659–664 (2000).
5. S. Leveque, A. C. Boccara, M. Lebec, and H. Saint-Jalmes, "Ultrasonic tagging of photon paths in scattering media: parallel speckle modulation processing," Opt. Lett. **24**, 181–183 (1999).
6. S. Sakadzic and L. V. Wang, "Ultrasonic modulation of multiply scattered coherent light: An analytical model for anisotropically scattering media," Phys. Rev. E **66**, 026603 (2002).
7. L. V. Wang, "Mechanisms of ultrasonic modulation of ultiply scattered light: an analytic model," Phys. Rev. Lett. **87**, 043903 (2001).
8. D. A. Weitz, J. X. Zhu, D. J. Durian, H. Gang, and D. J. Pine, "Diffusing-wave spectroscopy: the technique and some applications," Phys. Scr. **T49**, 610–621 (1993).
9. J. L. Harden and V. Viasnoff, "Recent advances in DWS-based micro-rheology," Curr. Opin. Colloid Interface Sci. **6**, 438–445 (2001).
10. D. A. Boas and A. G. Yodh, "Spatially varying dynamical properties of turbid media probed with diffusing temporal light correlation," J. Opt. Soc. Am. A **14**, 192–215 (1997).
11. D. A. Boas, L. E. Campbell, and A. G. Yodh, "Scattering and imaging with diffuse temporal field correlation," Phys. Rev. Lett. **75**, 1855–1858 (1995).
12. S. Sakadzic and L. V. Wang, "Correlation transfer and diffusion of ultrasound-modulated multiply scattered light," Phys. Rev. Lett. **96**, 163902 (2006).
13. S. Sakadzic and L. V. Wang, "Correlation transfer equation for ultrasound-modulated multiply scattered light.," Phys. Rev. E **74**, 036618 (2006).
14. C. U. Devi, R. M. Vasu, and A. K. Sood, "Application of ultrasound-tagged photons for measurement of amplitude of vibration of tissue caused by ultrasound: theory, simulation, and experiments," J. Biomed. Opt. **11**, 049802 (2006).
15. This perturbation approach is commonly used to solve the inverse paramater recovery problem. See, for example, H. M. Varma, B. Banerjee, D. Roy, A. K. Nandakumaran, and R. M. Vasu, "Convergence analysis of the Newton algorithm and a pseudo-time marching scheme for diffuse correlation tomography," J. Opt. Soc. Am. A **27**, 259–267 (2010).
16. A. Björck, *Numerical Methods for Least Squares Problems* (SIAM, 1989).
17. S. Sakadzic and L. V. Wang, "Correlation transfer equation for multiply scattered light modulated by an ultrasonic pulse," J. Opt. Soc. Am. A **24**, 2797–2806 (2007).
18. In general the measurement $F(p, \mathbf{r}, \omega_a) = |\tilde{F}(p, \mathbf{r}, \omega_a)|$. However, from the numerical simulations, for the objects we have chosen, we have noticed that the imaginary part of $\tilde{F}(p, \mathbf{r}, \omega_a)$ is negligible compared to its real part. Therefore, we have taken the measurement as $F(p, \mathbf{r}, \omega_a) \approx \tilde{F}(p, \mathbf{r}, \omega_a)$.
19. J. L. Lions, E. Magenes, and P. Kenneth, *Non-Homogeneous Boundary Value Problems and Applications* (Springer-Verlag, 1972), Vol. 2.
20. H. M. Varma, A. K. Nandakumaran, and R. M. Vasu, "Study of turbid media with light: recovery of mechanical and optical properties from boundary measurement of intensity autocorrelation of light," J. Opt. Soc. Am. A **26**, 1472–1483 (2009).
21. H. M. Varma, B. Banerjee, D. Roy, A. K. Nandakumaran, and R. M. Vasu, "Convergence analysis of the Newton algorithm and a pseudo-time marching scheme for diffuse correlation tomography," J. Opt. Soc. Am. A **27**, 259–267 (2010).